Fiber Optic Gyroscopes

Executive Summary

Fiber optic Gyroscopes (FOGs) use two beams of light which propagate simultaneously around a path of optical fiber to measure angular velocity. The rotation of the plane in which the optical fiber lies induces a phase difference between the two waves which is proportional to the angular velocity of the rotation. The optical waves fall onto a photoelectric sensor which produces a current dependent on the intensity of the light waves. The basic configuration of the FOG is inadequate as it fails at low velocities and also sets a high cap on the possible angular velocity. A better configuration using a modulating signal is discussed to resolve some of those problems, and a typical FOG from KVH Industries (RA2100) is discussed.

KVH fiber optic gyros, like the DSP-3000, offer the reliability, accuracy, and durability necessary to guide remotely operated and autonomous vehicles under water and on land.

Contents

1 Introduction

Measurement of angular velocity is useful in many different applications, from missile navigation to motion control as displayed in a Wiimote. There are three broad categories of possible sensors for angular velocity, Ring Laser Gyroscopes (RLG), Fiber Optic Gyroscopes (FOG) and MEMs based gyroscopes. The former two utilize the Sagnac effect (explained later) to measure angular velocity and are much more sensitive compared to MEMs gyroscopes. FOGs were developed in the 1980s as a more compact, albeit less sensitive, alternative to RLGs. Figure 1 juxtaposes the different technologies and names a few areas where they are used today. The high sensitivity of FOGs can allow it to determine the direction of the Earth's poles based solely on measurements of its angular velocity[1].

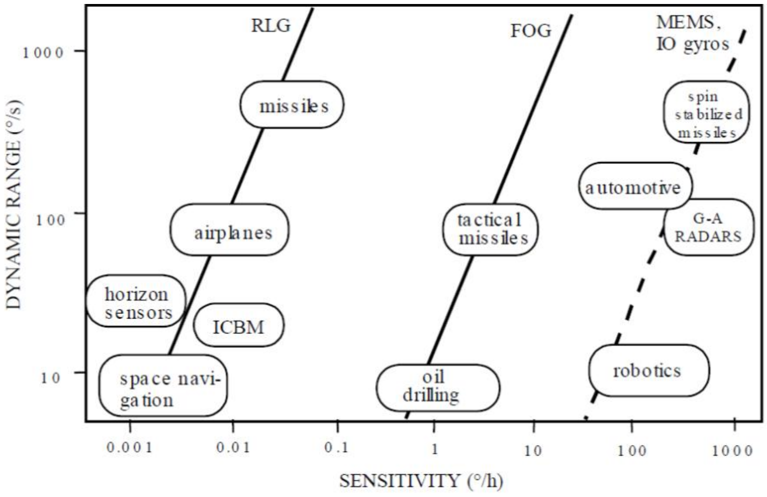

Figure 1: Applications areas for various gyroscope technologies, Laser Ring Gyroscopes, Fiber Optic Gyroscope and MEMs gyroscopes. [2]

As Figure 1 shows, FOGs are less sensitive than RLGs, but are more sensitive than MEMs gyroscopes. Interestingly, the three technologies are ranked in the same order in terms of compactness and cost, with the MEMs gyroscopes being the most compact and affordable. Since the three technologies are vastly different, they are used for widely different applications. However, as MEMs technologies improve, MEMs gyroscopes will become more competitive with performance to FOGs, as they are already competitive with respect to price [3].

2 Mode of operation

2.1 Classical explanation

The basic scheme of a fiber optic gyroscope is illustrated in Figure 2.

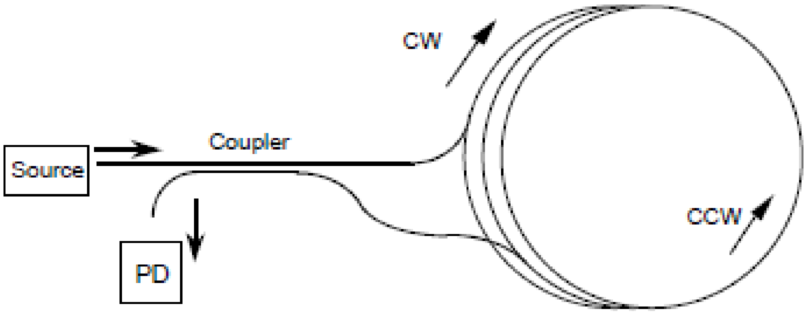

Figure 2: The Basic Configuration of a fiber optic gyroscope (FOG). [2]

It consists of a passive interferometer where a coupler is used to split the radiation from the light source into two counterpropagating waves, clockwise and counterclockwise, in the fiber coil and to recombine the waves, after propagation, on a photodetector (PD) [4, 5].

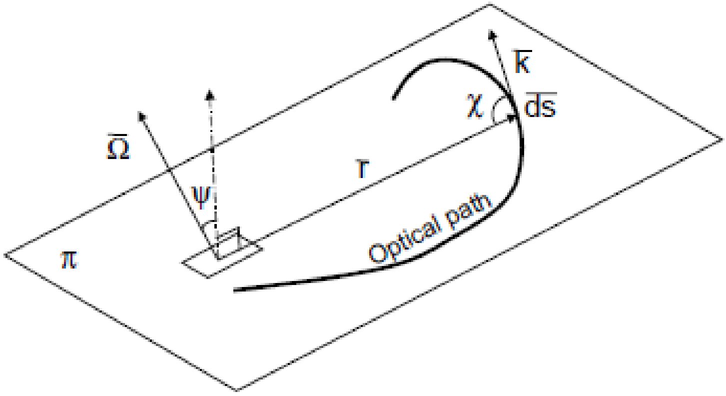

Figure 3: Geometrical representation of an optical path on a rotating plane for the Sagnac shift calculation. [2]

Using a long fiber coil wound into a coil, the phase difference is cumulated, obtaining high responsivity with a compact device. With ideal components, the output photogenerated current *I* has the following expression.

$$I = I_0(1 - \cos\theta_s)$$

where

$$I_0 = \frac{\sigma P}{2}$$

And σ is the photodetector responsivity and P is the power input from the source. To derive the expression for the Sagnac phase shift, an optical path lying on a plane can be considered, as shown in Figure 3. The π plane is rotating with angular velocity (Ω), which is orientated at an angle Ψ with respect to the perpendicular to the plane.

In the classical view, the rotation induces a Doppler frequency shift of the propagating optical wave. Considering the wave vector $\bar{k}$, propogating along an optical path $d\bar{s}$ produces a variation given by

$$\Delta k = k\frac{\bar{v}}{c}$$

where $\bar{v} = \bar{\Omega} \times \bar{r}$ and c is the speed of light. The optical phase shift $d\phi$ is then

$$d\phi = \Delta\bar{k} \cdot d\bar{s}$$

Substituting the above two equations yields

$$d\phi = \frac{[\bar{\Omega} \times \bar{r} \cdot d\bar{s}]k}{c}$$

Evaluating this based on the geometry from Figure 3,

$$d\phi = \left(\frac{k}{c}\right)\Omega cos\Psi r sin\chi \mathrm{ds}$$

Integration of the above along the entire optical closed path gives the total optical phase shift $\Delta\phi$

$$\Delta\phi = \left(\frac{k}{c}\right)\Omega cos\Psi 2AN$$

since the integration of $rsin\chi ds$ along the entire path length is $2AN$, where A is the area enclosed by the optical path and N is the number of turns. Considering that the Sagnac phase shift ϕ_s is the phase shift difference between two counterpropagating waves along the same optical path, $\phi_s = 2\Delta\phi$. In addition, since $k = 2\pi/\lambda$ the equation for the optical gyroscope can be obtained

$$\phi_s = \frac{8\pi AN\Omega_p}{\lambda c} \qquad \text{(Equation 1)}$$

which states that the Sagnac phase shift depends on $\Omega_p = \Omega\cos\Psi$, the component of the angular velocity perpendicular to the plane of the optical path. For the fiber optic gyroscope, N is the number of loops of the fiber coil and A is the area enclosed by each fiber loop.

2.2 Relativistic Explanation

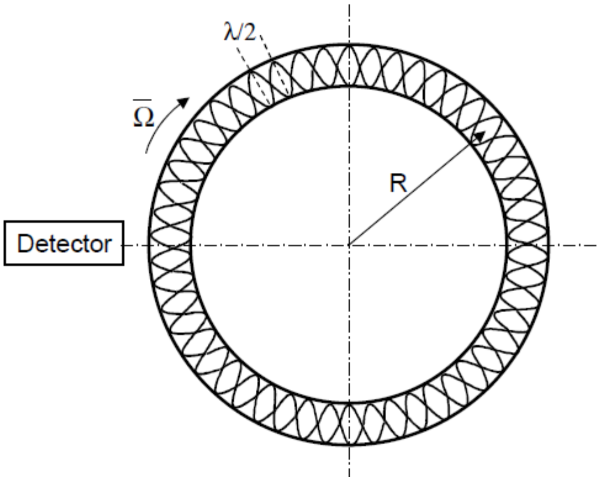

Figure 4: Standing wave in toroidal cavity rotating with the detector. [2]

In Equation 1, the vacuum wavelength λ is used, while classically the wavelength in the propagation medium is used. This is inaccurate because the observer(the photodetector) is accelerated and special relativity is required [6]. The relativistic explanation starts from a lossless, totally reflecting, toroidal, vacuum cavity where two counterpropagating waves form a standing wave with a $\frac{\lambda}{2}$ period as shown in Figure 4 [7]. Since there is no energy exchange between the cavity and the travelling waves, the generated standing wave is not affected by the angular rotation Ω_p of the cavity. For the observer rotating with the cavity, the standing wave seems to be moving with a velocity of $\Omega_p R$. This is equivalent to observing a frequency difference Δf between the counterpropagating waves given by

$$\Delta f = 2\Omega_p \frac{R}{\lambda}$$

Since there is resonance in the cavity, every c/p of frequency increase corresponds to a 2π increase in the optical phase shift, the Sagnac phase shift ϕ_s can be written as:

$$\frac{\phi_s}{2\pi} = \Delta f \frac{p}{c}$$

Where $p = 2\pi R$ is the perimeter, and thus ϕ_s is given by:

$$\phi_s = \frac{8\pi A\Omega_p}{\lambda c}$$

which is the same as Equation 1 if $N = 1$.

The relativistic analysis states that the above equation is correct when the detector is rotating with the gyroscope. However, if only the gyroscope or only the detector is moving, the above equation needs to be multiplied by n^2 or $n^2 - 1$ respectively [8]. In the practical case where the FOG fiber path is rotating while the observer is still, the new n^2 term cancels out with the n^2 coming from the factor $\lambda\, c$, and therefore the previous equation is valid also for a propagation medium with $n = 1$.

With a typical FOG (200 m-long fiber wounded on a 10 cm-diameter coil) the measurement of Earth's angular rotation $\Omega = 15°/h$ (required to detect a phase difference of $36\mu r$) corresponds to an optical path difference of the order of $10^{-12}m$. This measurement is to be performed in DC and thus it is considerably more difficult than the measurement of a tiny vibration in AC, as a low pass filter with a flat pass band region is required.

3 The open loop configuration with phase modulation

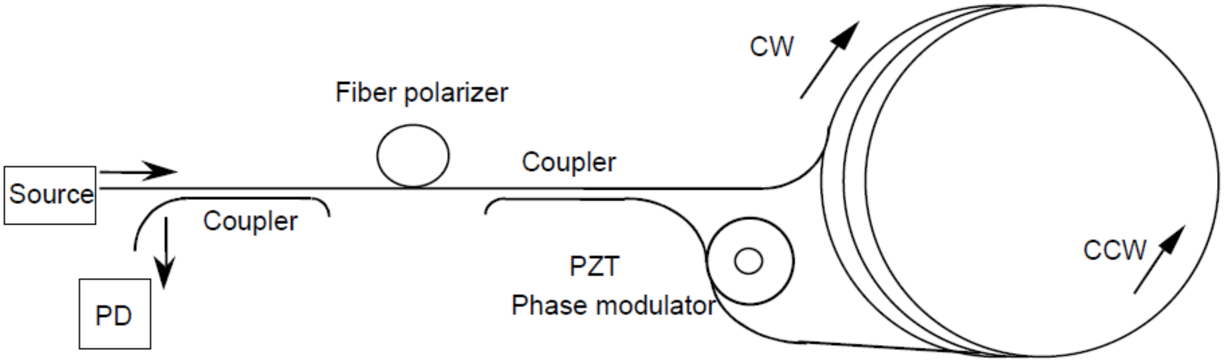

Figure 5: All fiber FOG with phase modulator.[2]

A major problem of the basic configuration is the output nonlinearity for small Sagnac shifts, which hinders high sensitivity measurements of small rotation angles without sign ambiguity ($\Omega_p = \Omega cos\Psi$ is even). This limitation is overcome using phase modulation, where the baseband cosine dependence is transformed into a sinusoidal function, by translating the output frequency from baseband to a carrier at angular frequency ω_m. This optical phase modulation technique is commonly used.

The typical setup uses a phase modulator inserted close to the coupler output, so that a different phase delay is cumulated by the counterpropagating waves [9]. The all fiber version of the phase modulator is constructed by winding and connecting a few fiber turns on a short hollow piezoceramic tube (PZT) [10]. By applying to the PZT a modulating voltage, a radial elastic stress and consequently optical pathlength variation due to the stress optic effect are generated.

As a result, the CCW and the CW propagating waves experience a phase delay $\phi(t)$ and $\phi(t+\tau)$ respectively, where $\tau = L/v$ is the radiation transit time in the fiber of overall length L. The relative path difference on the photo detector is then:

$$\phi_{CCW} - \phi_{CW} = \phi_S + \phi(t) - \phi(t+\tau)$$

which can also be written as

$$\phi_{CCW} - \phi_{CW} = \phi_S + \phi\left(t - \frac{\tau}{2}\right) - \phi(t + \frac{\tau}{2})$$

Applying a phase modulation at angular frequency ω_m

$$\phi(t) = \phi_{mo} cos\omega_m t$$

yields

$$\phi_{CCW} - \phi_{CW} = \phi_s + 2\phi_{mo} sin\omega_m \left(\frac{\tau}{2}\right) sin\omega_m t = \phi_s + \phi_m sin\omega_m t$$

where the amplitude of the phase shift can be maximized by selecting a PZT modulation frequency $f_m = \frac{\omega_m}{2\pi} = \frac{1}{2\tau}$.

Therefore, the photodetected signal is given by (using Bessel functions) [11]:

$$\frac{I}{I_0} = 1 + \left[J_0(\Phi_m) + 2\sum_{k-1}^{\infty} J_{2k}\,(\Phi_m) cos2k\omega_m t\right] cos\phi_s + \left[2\sum_{k-1}^{\infty} J_{2k-1}\,(\Phi_m)\cos(2k-1)\omega_m t\right] sin\phi_s$$

The photodetected signal contains, in addition to a DC component, all the harmonics of the modulating signal. The amplitude of the even harmonic components depends on $cos\phi_s$ as in the basic scheme, while the odd components carry the desired $\sin\phi_s$ dependence. The selection of of $\Phi_m = 1.8$ maximizes $J_1(\Phi_m)$ and the Sagnac phase shift with sign can be recovered by measuring the amplitude of the f_m frequency component of the photodetected signal.

4 Signal processing used

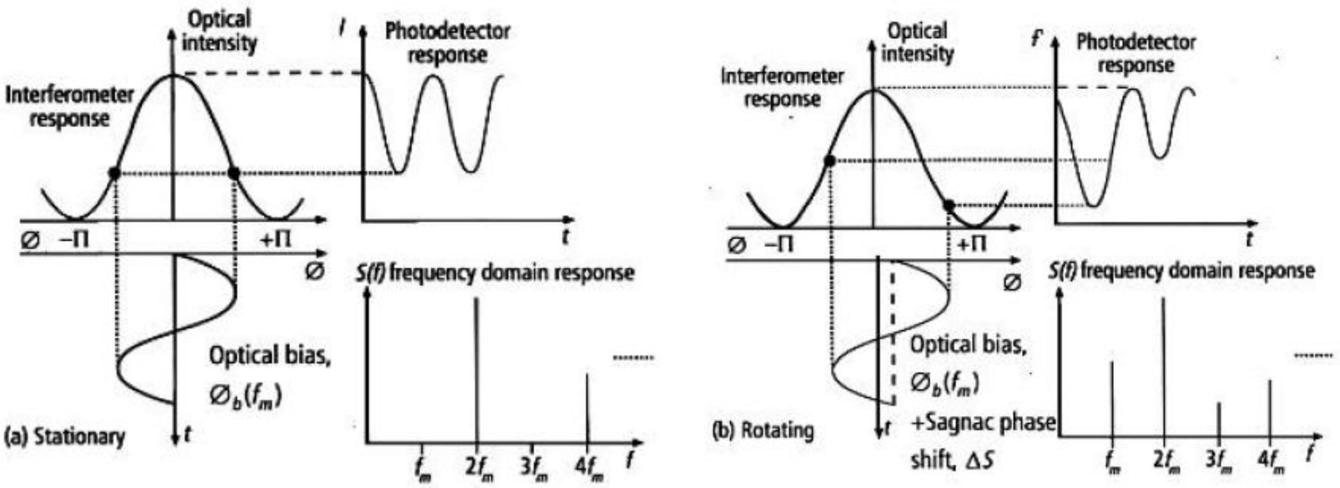

Figure 6: a) Photodetector output when the FOG is rotating and b) when rotating. [12]

Modulating the PZT with a sinusoidal voltage impresses a differential optical phase shift between the two light beams at the modulating frequency. The photodetector output for no coil rotation exhibits the periodic behavior of Figure 6a, whose frequency spectrum comprises of Bessel harmonics of the modulation frequency [12]. Since the phase modulation is symmetrical, only even harmonics are present. The ratio of the harmonic amplitudes depends on the phase modulation amplitude.

When the coil is rotated, the modulation occurs about a shifted position of the interferometer response. The phase modulation results in an unbalanced response and the fundamental and odd harmonics will also be present (Figure 6b). The amplitudes of the fundamental and odd harmonics are proportional to the sine of the angular rotation rate, while the even harmonics have a cosine relationship. Using the magnitude of the different frequency components, it is possible to extract the value of the Sagnac shift, and convert it into a meaningful angular velocity measurement [12].

4.1 Analog Implementation

An analog implementation of the signal processing apparatus includes an analog multiplier, a low pass filter, an oscillator, and the like which respond to the photoelectric output and generate a drive signal for the phase modulator [13].

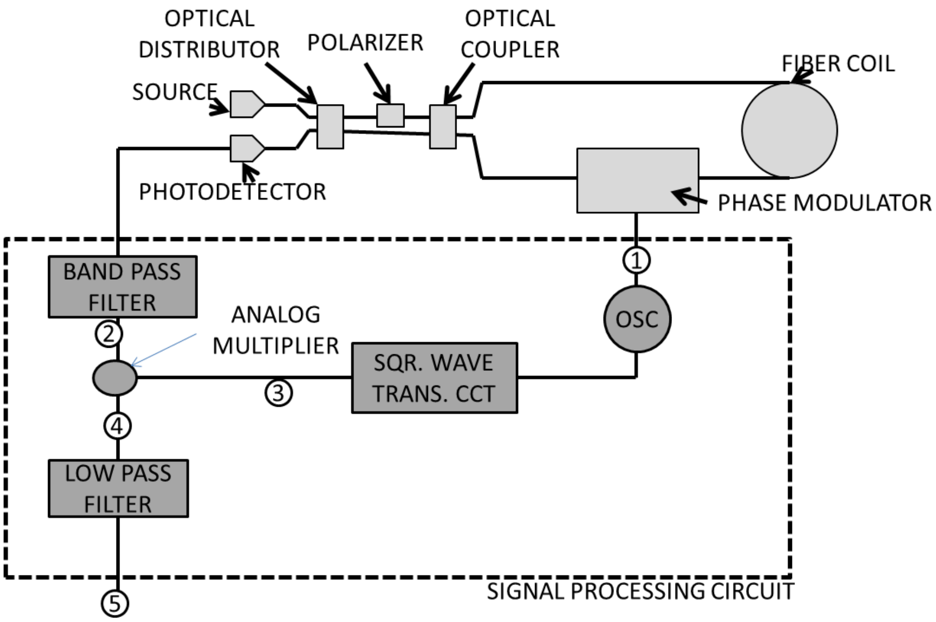

Figure 7: Light source, optical distributor and coupler, polarizer, phase modulator, optical fiber coil, photodetector, phase modulator output signal(1), band pass filter, analog multiplier, oscillator, a square wave transducing circuit and low pass filter. [13]

The band pass filter only transmits a component with the same frequency as the phase modulated signal. In addition, the phase modulated signal is driven by the oscillator which drives the square wave transducing circuit and produces a square wave which is synchronized in phase and frequency. Next the output signal of the square wave transducing circuit and the output of the band pass filter are fed into analog multiplier whose output is fed into a low pass filter. The result of the multiplier is only the positive component of the result from the band pass filter is transmitted to the low pass filter which only transmits the DC component, producing a voltage given by:

$$V_0 \propto -\left(\frac{2}{\pi}\right) P_o sin\phi_s J_1(\eta)\sin\Psi_0 + U_1 + U_2$$

Using such an analog demodulation has a number of drawbacks. Firstly, if the offset voltages occurring in each analog circuit fluctuate, the bias stability of the gyro is lowered. Another drawback is that the detectable angular velocity is limited to $\pm\frac{\pi}{2} rad$ with respect to the phase difference due to the Sagnac effect. Additionally, the linearity and scale factor stability of the gyro are easily deteriorated due to fluctuations in the intensity of the incident light on the photodetector. Furthermore, even if the input rotation velocity is zero, the bias stability of the gyro is easily lowered due to fluctuations in the offset voltages U_1 and U_2.

4.2 Digital Implementation

To overcome these limitations, a different digital signal processing apparatus can be used, as shown in Figure 8.

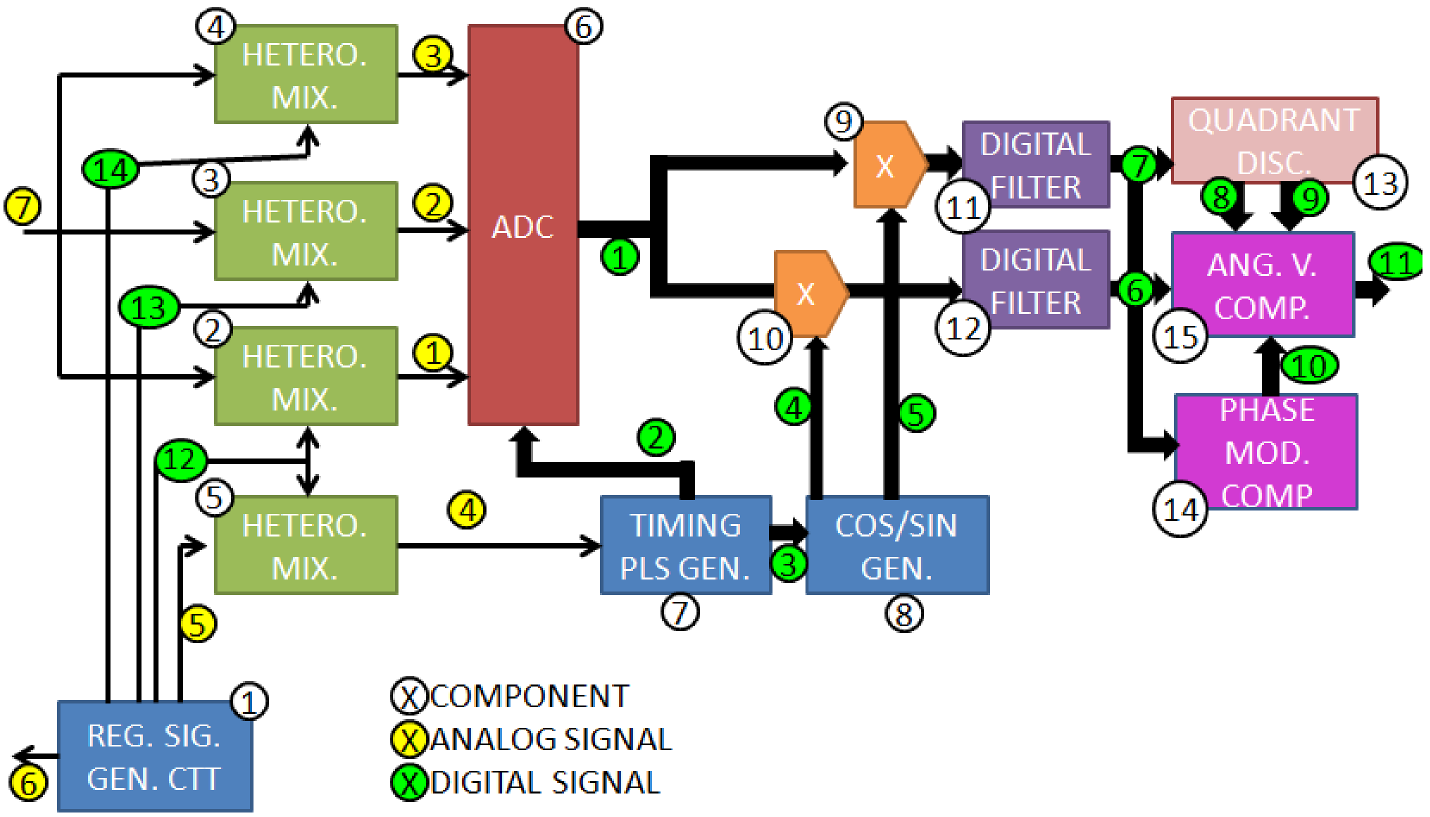

Figure 8: Digital signal processing apparatus. First to forth heterodyne mixers (2, 3, 4 and 5), an ADC (6), a timing pulse generating unit (7), a cosine/sine signal generating unit (8), first and second digital multipliers (9, 10), first and second digital filters (11, 12), a quadrant discriminating unit (13), an angular velocity computing unit (15), a phase modulation index computing unit (14) and a reference signal generating circuit (1). [13]

The reference signal generating circuit outputs a phase modulator drive signal and generates a fifth analog signal, a twelve digital signal, a thirteenth digital signal, and a fourteenth digital signal synchronized in frequency and phase with the sixth analog signal.

The first heterodyne mixer responds to the twelfth digital signal, and takes a signal component of the same frequency as a frequency of the phase modulator drive signal from the photoelectric output signal, and converts the signal component to a signal of frequency Δfm and outputs a first analog signal which is expressed by:

$$V_1 \propto 2P_0 sin\phi_s J_1(\eta)\sin(2\pi\Delta fmt+\psi_1)$$

The second heterodyne mixer responds to the thirteenth digital signal, takes a signal component of frequency $2fm$ from the photoelectric output signal and converts the signal component to a signal of frequency Δfm and outputs a second analog signal (16) given by :

$$V_2 \propto 2P_0 cos\phi_s J_2(\eta)\sin(2\pi\Delta fmt+\psi_2)$$

Similarly, the third heterodyne mixer responds to the signal component at $4fm$ and produces an analog voltage:

$$V_3 \propto 2P_0 sin\phi_s J_4(\eta)\sin(2\pi\Delta fmt+\psi_3)$$

ψ_1, ψ_2 and ψ_3 correspond to a phase difference between the signal component of the input frequency (fm, $2fm$ and $4fm$) and the driving digital signals ($fm+\Delta fm$, $2fm+\Delta fm$ and $4fm+\Delta fm$).

The fourth heterodyne mixer converts the fifth analog signal to a signal of frequency Δfm and outputs the fourth analog voltage which is expressed by:

$$V_4 \propto \sin(2\pi\Delta fmt + \psi_{\mathrm{REF}})$$

ψ_{REF} represents the phase difference between the fifth analog signal and the twelfth digital signal. Note that $2\pi\Delta fm = \Delta\omega_m$.

The fourth analog signal is input to the timing pulse generating unit (7) and is used to drive the second and third digital signals. The second digital signal is input to the ADC (6) which converts the first to third analog signals to the first digital signal in synchronization with the second digital signal.

The third digital signal is input into the cos/sin generating unit (8) which divides one cycle of the signal into timeslots at every predetermined time and outputs values of cosine and sine, which are generated at times corresponding to the time slots and shifted in phase by $90°$ from each other. The values of sine and cosine are output as fourth and fifth digital signals expressed by:

$$V_{REF,cos} \propto \cos(\Delta\omega_m t + \psi_{\mathrm{REF}})$$

$$V_{REF,sin} \propto \sin(\Delta\omega_m t + \psi_{\mathrm{REF}})$$

The forth digital signal together with the first digital signal is input to the first digital multiplier. The first digital filter (11) is a low pass filter which takes the DC component from the multiplier and produces the sixth digital signal.

Similarly, the seventh digital signal is produced using the fifth and first digital signal.

The sixth and seventh digital signals are fed into the quadrant discriminating unit. The quadrant discriminating unit executes logic based on the signs of the components of the sixth and seventh digital signals. The phase difference due to the Sagnac effect is broken down into $\frac{\pi}{2}$ increments which are given different quadrant values from zero to three (A two bit digital signal). This allows the device to determine when the signal shifts between different quadrants, as the value of the eighth digital signal will change. Through some clever logic, the changes in quadrants can be tracked and translated into the ninth digital signal which associates each range of 2π in Sagnac shift with an integer.

The phase modulation computing unit (14) executes the computation below based on the components $V_{2,cos}$ and $V_{3,cos}$ of the sixth digital signal and the components $V_{2,sin}$ and $V_{3,sin}$ of the seventh digital signal indicated by the formula:

$$g\left[V_{2,cos}^2 + V_{2,sin}^2\right)^{\frac{1}{2}} / \left(V_{3,cos}^2 + V_{3,sin}^2\right)^{\frac{1}{2}}] = g[|\frac{J_2(\eta)}{J_4(\eta)}|] = |J_2(\eta)/J_1(\eta)|$$

Note that $g[\,]$ represents a function $|\frac{J_2(\eta)}{J_4(\eta)}|$ to $|\frac{J_2(\eta)}{J_1(\eta)}|$.

The phase modulation index computing unit (14) outputs a tenth digital corresponding to the computed value shown by the above formula.

The angular velocity computing unit (14) executes the computation below based on the components $V_{1,cos}$ and $V_{2,cos}$ of the sixth digital signal and the components $V_{1,sin}$ and $V_{2,sin}$ of the seventh digital signal and the tenth digital signal.

$$Q = \left|\frac{J_2(\eta)}{J_1(\eta)}\right| \times \left[\frac{\left(V_{1,cos}^2 + V_{1,sin}^2\right)^{\frac{1}{2}}}{\left(V_{2,cos}^2 + V_{2,sin}^2\right)^{\frac{1}{2}}}\right] = |\tan(\phi_s)|$$

The angular velocity computing unit (15) responds to the computed value shown by the equation above and the eighth and ninth digital signals to compute the phase difference based on the Sagnac effect and outputs an eleventh digital signal corresponding to the computed phase difference.

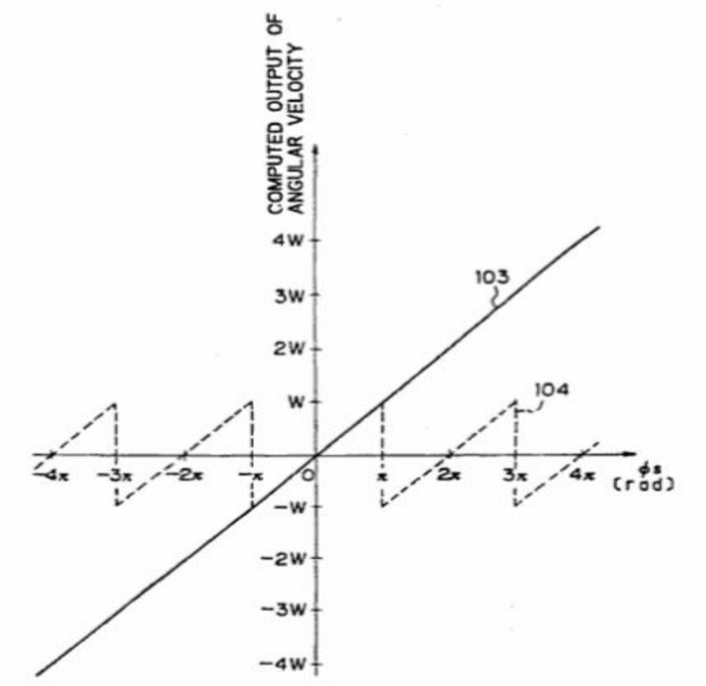

Figure 9: Computed values in the angular velocity computing unit based on the values of the eighth and ninth digital signals and the extraction of ϕ_s from Q. [13]

Depending on the value of the eighth digital signal, a different offset is added to the value. For instance, if the value from the eighth digital signal is 2, the phase shift could be in the range of 0 to $\frac{\pi}{2}$. If the tangent of the phase shift is smaller than 1, the phase shift is simply run through an arctangent operation to recover the phase shift. However, if the tangent of the phase shift is greater than 1, the arctangent of the inverse is taken and subtracted from $\pi/2$. This is to improve the sensitivity of the device. For instance, if the phase shift decreased 2% from $\pi/2$, the tangent would decrease by 1.6×10^{16}. This would be difficult to detect without a very large number of bits in the digital signal which is not practical. However, if we invert the value then take the arctangent of it, the change is a much more reasonable 0.02. Therefore, by using different processing if the tangent of the phase shift is above or below 1, the sensitivity of the readings can be improved.

After that, the value of the ninth digital signal is used to correctly scale the phase shift depending on the number of complete 2π shifts the Sagnac shifts represents. This is represented by the value of the ninth digital signal. If the phase shift is calculated to be $\pi/3$ and the ninth digital signal is 4, the value of the Sagnac shift is $\frac{25\pi}{3}$.

This signal chain produces an accurate gyro output signal in proportion to the input rotation angle and expands the maximum range of detection of the angular velocity. Also, it is possible to perfectly remove various influences by fluctuating the quantity of incoherent light of the light beam incident on the photoelectric transducing circuit, fluctuating in the phase modulation index, or fluctuating the phase difference between the photoelectric output signal and the phase modulated drive signal. As a result, the linearity and scale factor stability of the gyro are improved.

Furthermore, the signal components of fm, $2fm$, and $4fm$ taken out of the photoelectric output signal (analog signal 7) by the first to third heterodyne mixers are converted by the A/D converter to the first digital signal which is then digitally demodulated by the digital multipliers and the digital filters. Accordingly, it is possible to prevent an occurrence of offset voltages due to an analog demodulation. This contributes to an improvement in the bias stability of the gyro.

5 Quantum Theoretical Performance Limit

Considering the phase signal detected by the FOG, the phase noise ϕ_n detected at the quantum limit is equal to the inverse of the amplitude of the signal to noise ratio calculated at the bias point $\phi_{sb} = \pi/2$[14]. Considering the signal current I_0 and the related shot noise current, $I_{shot} = \sqrt{2eI_0B}$, where B is the measuring bandwidth and e is the electron charge, the phase noise is:

$$\phi_n = \frac{I_{shot}}{I_0} = \sqrt{\frac{2eB}{I_0}}$$

which can be stated alternatively as:

$$\phi_n = \sqrt{\frac{2hfB}{P_0}}$$

since

$$I_0 = \frac{e}{hf} P_0 \eta$$

where h is the Planck's constant, $f = \frac{c}{\lambda}$, P_0 is the equivalent detected power and η is the quantum efficiency of the photodetector. The phase noise at the quantum limit corresponds to a noise equivalent rotation rate $NE\Omega$ given by

$$NE\Omega = \frac{\lambda c}{8\pi AN} \sqrt{\frac{2hfB}{P_0 \eta}}$$

The phase noise at the quantum limit as a function of bandwidth, B, is shown, with the equivalent detected power P_0 as a parameter. For example, for B=1 Hz and $P_0 = 0.1mW$ the phase noise is $\phi_n = 5 \cdot 10^{-8} rad$, corresponding to a minimum detectable angular velocity of $34 \cdot 10^{-9} rad/s$, which is a very good value that is not attained in practice.

There are several non-idealities preventing the FOG from reaching the ultimate quantum noise limit, all studied in detail but none completely explaining the observed data. We will comment on them in the following section, while discussing the individual components and readouts of the gyro.

Concerning the propagation medium, i.e., the fiber, phase noise due to thermodynamic fluctuations of the fiber refractive index and length has been investigated [15]. In a Sagnac configuration, however, this noise contribution becomes important only at relatively high input powers (say ~20 mW, for which n~10-8 rad/√Hz) and is not therefore the dominant extra noise term. Since both the CW and CCW waves travel through the same optical path, the experience the same amount of noise due to changes in the fiber, minimizing that noise contribution.

6 Problems of development

Ultimately, it is necessary to eliminate all the sources of nonreciprocity (different optical path lengths), other than that induced by the Sagnac effect, in the propagation of the CW and CCW waves. All other sources of nonreciprocity contribute to noise in the reading of the Sagnac shift, deteriorating the quality of the instrument.

If the counterpropagating waves cumulate a nonreciprocal phase shift due to the optical components or ambient-induced disturbances (temperature fluctuations), zero-point errors and fluctuations will occur [16]. Significant errors are caused if the counterpropagating waves do not travel along the fiber with the same state of polarization and the same modal distribution.

To minimize the problem of polarization, special fibers as well as optical modal filters and polarization controllers are employed for the FOG. A single polarization interferometer is obtained using high-birefringence fiber for the measuring coil with one or more polarizers. In another typical implementation, single mode low-birefringence fiber is used and care must be taken to avoid bending induced birefringence. The use of all fiber components is recommended to eliminate reflections and modal conversion which usually occur at the interfaces of bulk optical components [17].

Reciprocity also requires that radiation travel symmetrically through all of the optical components. In the basic setup, a nonreciprocity arises because, with a single coupler, the CCW wave is cross coupled twice while the CW wave is bar coupled twice. A fluctuation of the coupling ratio and hence of the coupling phase shift thus fully affects the Sagnac signal. By noting that the light coming out from the coupler and directed toward the source is composed by CW and CCW contributions that have both experienced a crossed and a bar coupling, it is straightforward to correct the launch-coupler non-reciprocity by adding a second coupler [18].

Another source of errors is backscattering, which induces crosstalk between the CW and the CCW waves [19]. In the FOG, scattering usually includes Rayleigh backscattering as well as backreflection at the interfaces. This problem can be solved by using a light source with a very short coherence length, which prevents beating effects between the backscattered component and the copropagating wave [20]. A superluminescent diode is thus the best choice for satisfying this requirement and for ensuring at the same time high coupling efficiency in the single mode fiber.

The magneto-optical Faraday effect is another nonreciprocal effect potentially dangerous in addition to the Sagnac effect [21]. The effect can cause the polarization of the optical waves to change as they move through the optical path. This problem is now almost solved by the use of carefully untwisted polarization-maintaining fibers. Similarly, the nonreciprocity induced by the nonlinear Kerr effect can be reduced with broadband, low coherence, unpolarized optical sources or even with a simple 50% duty cycle modulation of the input optical power [22].

7 Case Study (RA2100 – KVH Industries)

As an example, the RA2100 from KVH industries was studied. It is a single axis FOG which was developed in the 1990s. It operates at an optical wavelength of 820nm with a 75 meter coil of fiber. It uses the analog electronic signal chain described previously, which makes the output susceptible to bias offset, scale factor nonlinearity and stability, bias stability and a random noise component [12].

This short coil length results in operation in the linear portion of the sine responses curve, improving the linearity of the gyro. The sensitivity of the gyroscope depends on the optoelectronic noise, which is broadband and inversely proportional to the optical power, and the Sagnac scale factor, which is the proportionality between angular rate and the optical phase shift. In addition, the performance depends on the demodulation approach chosen. Since many applications are exposed to the environment, performance as a function of temperature is a significant factor. More important than the variation of parameters with temperature is repeatability, as many system applications employ individually modeled corrections as a function of temperature and rate.

The variation of bias versus temperature is shown below.

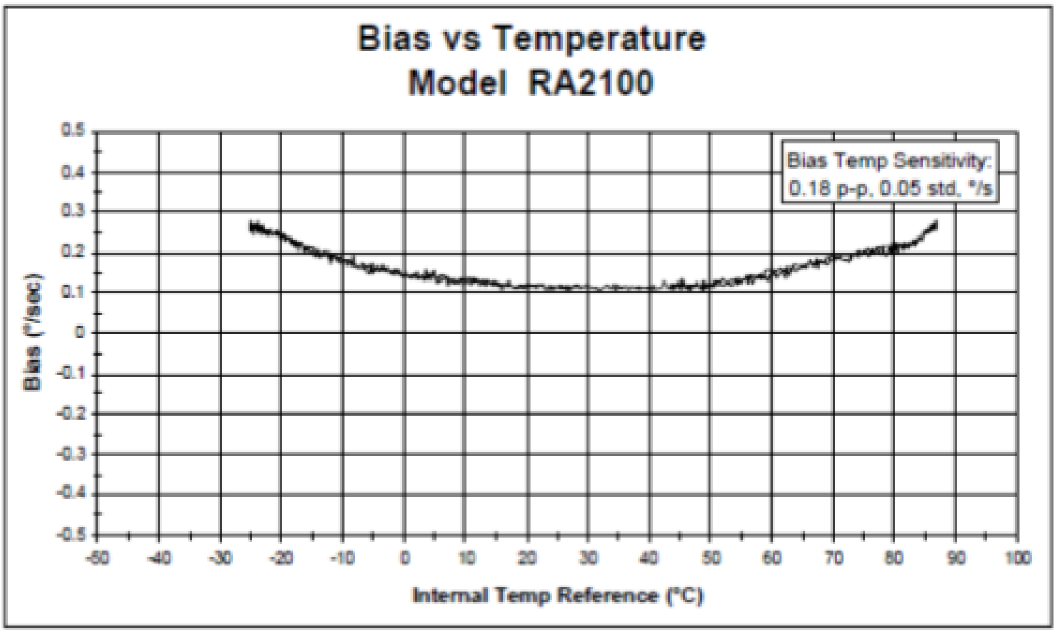

Figure 10: Bias variation over the full temperature range. It is slowly varying and repeatable. [12]

The data were obtained by ramping a thermal chamber with a dwell at the maximum and minimum temperatures. The bias is observed to vary slowly, and the results are repeatable. As mentioned previously, the best bias performance is obtained when the modulation frequency is equal to half the transit time of the light through the coil. This helps to suppress the second harmonic effects. It was determined that the bias effect is mainly due to the DC offset of the operational amplifiers used to amplify the signal after the demodulation. The larger was the range of the signal, the larger the amplification, and thus the larger the susceptibility to offsets.

The input/output rate relationship is shown below to have excellent linearity using a simple demodulation technique. The data shown are for an analog output, and the left hand scale represents the output voltage as a function of input rotation rate.

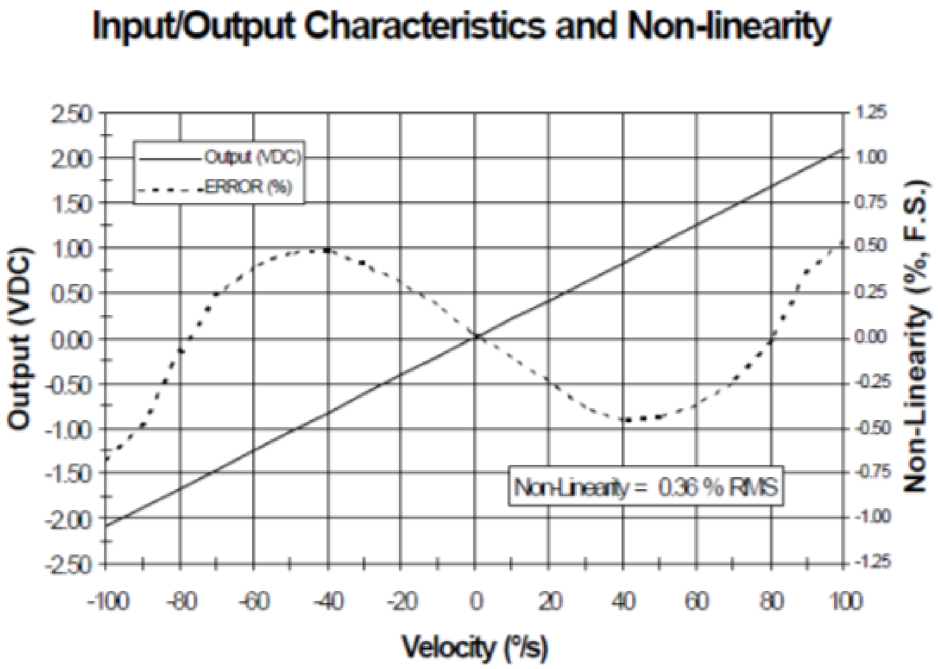

Figure 11: Input-Output Characteristics and Non-Linearity for RA2100. [12]

The underlying cause of the nonlinearity is the sinusoidal response of the Sagnac interferometer which is being approximated as linear. The gyro therefore exhibits an increasing nonlinearity as the rate increases. For high rates, a systematic deviation from linearity occurs.

The overall relationship of the input rate to output voltage is the scale factor, which is proportional to the Sagnac phase shift. However, the constancy of the scale factor depends on the modulation depth and optical power being constant over temperature and time. Since that is not the case, there is a 2.4% variation in the scale factor within the operational range of the sensor.

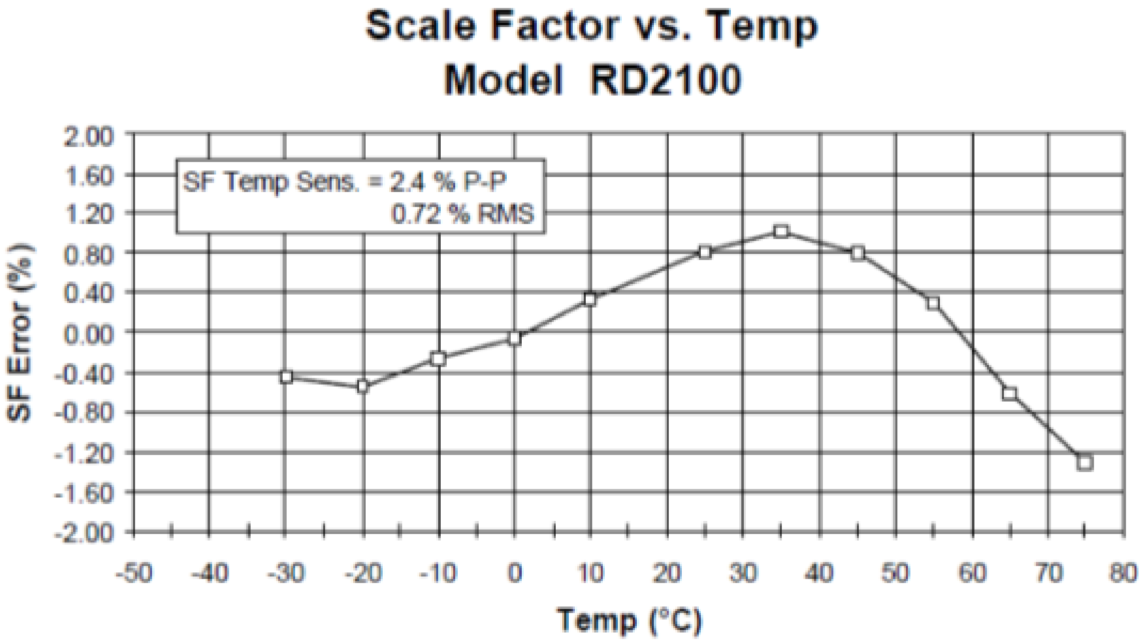

Figure 12: Scale factor versus temperature. Scale factor is a good measure for the overall input to output relationship. [12]

Finally, the overall stability of the gyro is best characterized by Allan variance statistics [23], shown in the figure below.

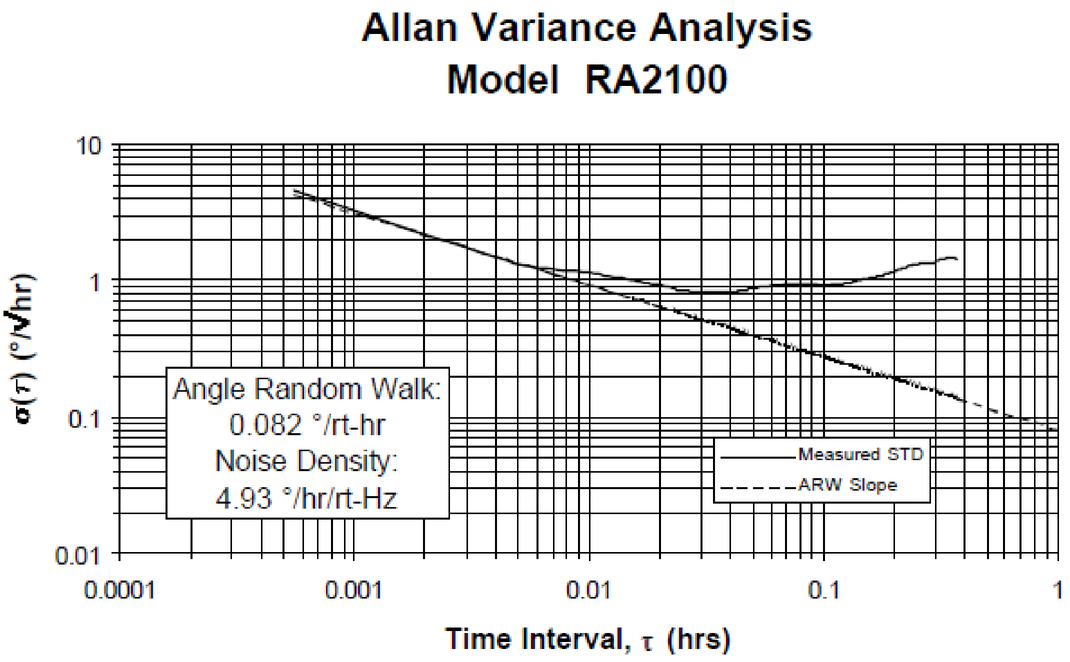

Figure 13: Allan Variance analysis which is a measure of Angle Random Walk and bias instability. [12]

This measurement is performed at a fixed temperature and can be interpreted to determine the Angle Random Walk (ARW) and bias instability. Typically, the square root of the Allan variance is plotted and the region of short time differences, τ, is characterized by a slope of $-1/2$. The intercept of the slope with the one hour line yields the angle random walk in $\circ/\sqrt{h}$, which can also be expressed as a noise power spectral density. This is obtained by multiplying the value by a factor of 60, transforming the units to $(\circ/h)/\sqrt{Hz}$. This noise is a function of the coil length and the optical source. As the bias instability represents the best performance of the gyro after the angle random walk is eliminated by averaging, the ARW is a measure of how well one can measure the bias offset of the gyro for purposes of modeling.

8 Conclusion and future work

Fiber Optic Gyroscopes are robust apparatus for measuring angular velocity. Beyond the open loop configuration mentioned here, there are other configurations that incorporate feedback to minimize the effects of bias offsets and ARWs. These techniques help to make the FOG more reliable as a sensor. It is interesting that the FOG is an instrument where merely improving the processing of the incoming sensor signal can yield more stability, linearity and sensitivity.

9 References

1. TANAKA,T., IGANNISHI,Y., MAKOTO,N., and YOSHIN0.T.: 'Auto north sensor using a fiber optic gyroscope', Appl. Opt., 1994, 33, (I), pp. 12CL123
2. López-Higuera, J. Handbook of Optical Fibre Sensing Technology. New York: Wiley, 2002
3. Product Design and Development, Inc ,"Silicon Sensing's MEMs Gyro Enables North-Seeking," June 2009 [Online] Available: http://www.pddnet.com/news-silicon-sensings-mems-gyro-enables-north_seeking-063009/ [Accessed Mar 18 2010]
4. V. Vali, R. W. Shorthill, 'Fiber Ring Interferometer, Appl Optics', 15 (1976), pp 1099-100
5. S. Donati, 'Il giroscopip elettroottico: stato dell'arte e prospettive', Alta Frequenza, Vol 2, 1990, pp. 143-54
6. J. Van Blanden, Relativity and Engineering, Springer Verlag, 1984

7. E. O. Schulz DuBois, ‘Alternative Interpretation of Fresnel-Fizaeu Effect in Rotating Optical Fiber Ring Interferometer’, Appl Opt. 16 (1977), pp. 2605-7.
8. V. Vali, R. W. Shorthill, and M. F. Berg, "Fresnel-Fizeau effect in a rotating optical fiber ring interferometer," Appl. Opt. 16, 2605-2607 (1977)
9. Ezekiel, S., and H. J. Arditty, ‘Fiber-optic rotation sensors and related technologies”, Springer Verlag, Berlin, 1982
10. G. Martini, ‘Analysis of a single mode optical fibre piezoceramic phase modulator’, J. Opt. Quantum Electron., Vol. 19, 1987, pp. 179-90.
11. Efunda, Inc ,”Bessel Function,” March 2010. [Online] Available: http://www.efunda.com/math/bessel/bessel.cfm. [Accessed: Mar 17 2010]
12. Bennett, S. M., R. Dyott, D. Allen, J. Brunner, R. Kidwell, and R. Miller. "FIBER OPTIC RATE GYROS AS REPLACEMENTS FOR MECHANICAL GYROS." American Institute of Aeronautics and Astronautics 4401st ser. (1998). Print.
13. Kurukawa, Akihiro, Hiroshi Narise, and Takafumi Hirano. Signal Processing Apparatus for Optical Gyro. Mitsubishi Precision Co. Ltd, Tokyo, Japan, assignee. Patent 5289257. 22 Feb. 1994. Print.
14. Special Issue on gyroscopes and monomode optical components, IEE Proc. J, Vol. 132, pp. 249-308
15. V. Annovazzi, S. Donati, S. Merlo, ‘Thermodynamic phase noise in fibre interferometers, Optical and Quantum Electronics’, vol. 28, 1996, pp. 43-9.
16. Ulrich, R., ‘Fiber-optic rotation sensing with low drift’, Opt. Lett., Vol. 5, 1980, pp. 173–5.
17. Moeller, R. P., W. K. Burns, and N. J. Frigo, ‘Open-loop output and scale factor stability in a fiber-optic gyroscope’, IEEE J. Lightwave Technol., Vol. LT-7, 1989, pp. 262–9
18. Bergh, R. A., H. C. Lefevre, and H. J. Shaw, ‘All single mode fiber optic gyroscope’, Opt. Lett., Vol. 6, 1981, pp. 198–200.
19. Cutler, G. C., S. A. Newton, and H. J. Shaw, ‘Limitation of rotation sensing by scattering’, Opt. Lett., Vol. 5, 1980, pp. 488–90.
20. Bergh, R. A., H. C. Lefevre, and H. J. Shaw, ‘All single mode fiber optic gyroscope with long term stability’, Opt. Lett., Vol. 6, 1981, pp. 502–4.
21. Hotate, K., ‘Noise sources and countermeasures in optical passive ring-resonator gyro’, Proc. OFS 7, 1990, pp. 11–42.
22. Frigo, N. J., H. F. Taylor, L. Goldberg, J. F. Weller, and S. C. Rashleigh, ‘Optical Kerr effect in fiber gyroscope: effects of nonmonochromatic sources’, Opt. Lett., Vol. 8, 1983, pp. 119–21.
23. IEEE Std. 952-1997 “IEEE Standard Specification Format Guide and Test Procedures for Single-Axis Interferometric Fiber Optic Gyros” IEEE Standards, Piscataway, NJ, USA, 1998